Aerodynamic and aeroacoustic comparison of optimized high-speed propeller blades

Aerodynamic and Aeroacoustic Comparison of Optimized High-Speed Propeller Blades

Alexandre Capitao Patrao*, Daniel Lindblad†, Anders Lundbladh‡, and Tomas Grönstedt §
Chalmers University of Technology, Göteborg, Sweden, 412 96

The Boxprop is a high-speed propeller concept intended for aircraft engines, which features blade pairs connected at the tip in order to decrease tip vortex strength, possibly reducing noise and improving aerodynamic performance relative to conventional high-speed propellers. This paper investigates the aerodynamic and aeroacoustic performance of three aerodynamically optimized high speed propellers; a 6-bladed conventional propeller, a 12-bladed conventional propeller, and a 6-bladed Boxprop. Performance results will be be compared for the three designs, with a focus on sectional performance and wake flow characteristics, and will show that the 6-bladed Boxprop performance lies somewhat in-between its 6 and 12-bladed conventional counterparts. The noise level at various observer positions is presented, and shows that the noise roughly follows the values of efficiency for the three propellers, with the Boxprop noise level being higher than the 12-bladed conventional propeller, but lower than the 6-bladed one. The lower blade loading and higher efficiency of the Boxprop relative to the 6-bladed conventional propeller results in slightly lower levels of noise at cruise.

Nomenclature

B	=	Number of blades
$CROR$	=	Counter-Rotating Open Rotor
C_T	=	Coefficient of thrust = $T/\left(\rho_\infty n^2 D^4\right)$
c	=	Airfoil chord, m
d_i	=	Blade passage distance for stacking line control point P_i, m
D	=	Diameter, m
FR	=	Frozen Rotor interface
GA	=	Genetic Algorithm
h	=	Flight altitude, m
H	=	Axial distance measured from a point located at the TE of the LB at 75% radius, m
HTR	=	Propeller Hub-to-Tip Ratio
L'	=	Propeller sectional lift, N/m
LB	=	Leading Blade
M_∞	=	Freestream Mach number
n	=	Blade revolutions per second, 1/s
P_i	=	Stacking line control point
P_{shaft}	=	Propeller shaft power, W
r	=	Radius, m
R	=	Propeller tip radius,m
SPL	=	Sound Pressure Level, dB
OF	=	Objective function of the optimization
t	=	Airfoil profile thickness, m

*PhD Student, Department of Mechanics and Maritime Sciences (M2), Chalmers University of Technology, Hörsalsvägen 7a, 412 96 Göteborg, Sweden.

†PhD Student, Department of Mechanics and Maritime Sciences (M2), Chalmers University of Technology, Hörsalsvägen 7a, 412 96 Göteborg, Sweden.

‡Adjunct Professor, Department of Mechanics and Maritime Sciences (M2), Chalmers University of Technology, Hörsalsvägen 7a, 412 96 Göteborg, Sweden.

§Professor, Department of Mechanics and Maritime Sciences (M2), Chalmers University of Technology, Hörsalsvägen 7a, 412 96 Göteborg, Sweden.

T	=	Propeller thrust, N
T'	=	Propeller sectional thrust,N/m
TB	=	Trailing blade
TE	=	Trailing edge
V_∞	=	Freestream axial velocity, m/s
$V_{\infty,r}$	=	Freestream axial velocity in the rotating frame of reference, m/s
ρ_∞	=	Freestream density, kg/m^3
ϵ	=	Lift-to-drag ratio
κ_i	=	Chord displacement angle [°]
η_{prop}	=	Propeller efficiency = TV_∞/P_{shaft}

I. Introduction

The growth trend seen in air travel over the last half-century is not expected to halt anytime soon, but economic, environmental, political, and consumer pressure is forcing aero engine manufacturers to develop more radical approaches to reduce fuel consumption and emissions. One of these approaches is the Open Rotor, which promises a significant fuel reduction relative to the turbofan [1]. Open Rotor designs from the 1980s suffered from high noise levels, but more recent designs have managed to lower the noise levels [2] by employing blade clipping [3–5], varying rotational velocity and blade clipping [6], aeroacoustic blade shape optimization [7, 8], and serrated trailing edges [9]. An alternative approach may lie in using the Boxprop propeller concept [10–12], which features pair-wise blades connected at the tip, forming a continuous blade arch, see Fig. 1a. Connecting the *leading blade* (LB) to the *trailing blade* (TB) is hypothesized to lead to a weaker tip vortex and a more rigid mechanical structure, possibly decreasing the risk for flutter and allowing forward-sweeping of the blades.

Early optimization attempts [13] of the Boxprop with a low number of design variables demonstrated the usefulness of the developed optimization platform, allowing interesting new Boxprop geometries and modest increases in efficiency. Since then, several aerodynamic optimizations have been carried out with increasing number of design variables, thereby increasing the design space incrementally.

A key design parameter for the Boxprop is the optimal number of blades. From an aerodynamic point-of-view only, and for a given propeller activity factor, a propeller rotor should strive for as many blades as possible, since this increases the induced efficiency of the propeller. From a structural mechanics point-of-view, a high number of thin blades with low chord values would lead to high blade stresses and an increased risk for flutter [4]. For the Boxprop, there is an additional limit set by the space required by the blade pitching mechanism compared to a conventional blade. Moreover, a Boxprop with B number of Boxprop blades can be argued to have either B or $2B$ propeller blades, depending on if the leading and trailing blades are seen as two separate blades, or as one single blade.

This paper strives to find the equivalency in blade count between the Boxprop and conventional high-speed propeller blades by comparing their aerodynamic performance and aeroacoustic impact. This is done by analyzing the three types of propellers shown in Fig. 1; a 6-bladed Boxprop, a 6-bladed conventional propeller, and a 12-bladed conventional propeller. These propellers are the result of a meta-model assisted, multi-objective optimization utilizing the NSGA-II Genetic Algorithm (GA) [14]. Aerodynamically optimized designs of each type will be compared for the cruise operating point and a thrust coefficient which is representative of the front rotor of a modern Counter-Rotating Open Rotor (CROR).

II. Methodology

A. Propeller specification

The main propeller design parameters shared among the three propeller types studied in this paper are shown in Table 1. For the Boxprop, the chord, camber, and angle-of-attack distributions are parametrized using 2D Beziér curves when constructing its NACA16 airfoil sections. The airfoil sections resulting from these distributions are then placed on stacking lines composed of 3D Beziér curves, allowing the leading and trailing blades to be forward and rear-swept, respectively. The stacking line Beziér curves are defined using control points P_i, as is shown in Fig. 2. In turn, the control points are defined using a blade passage distance d_i and a chord displacement angle κ_i, which control the spacing and angle between the blade halves, respectively. Positive values κ_i results in the LB being sheared/swept downstream,

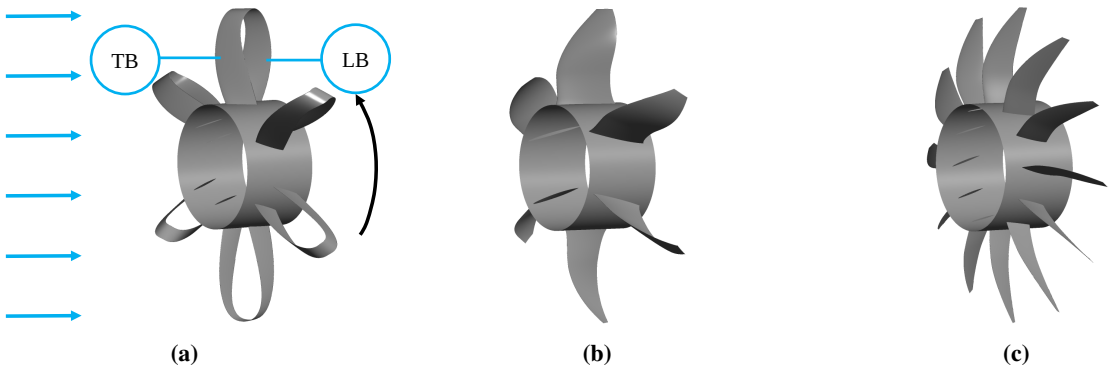

Fig. 1 a) Boxprop propeller concept with inflow (blue arrows) and rotational direction (black arrow). Leading and trailing blades are in reference to the rotational velocity. The optimized 6 and 12-bladed conventional propellers are shown in b) and c).

while the TB is sheared/swept upstream. In total, 32 design variables are required for defining the Boxprop. For a complete description of the Boxprop parametrization, geometry generation, and mesh generation, see [13].

For the conventional propeller blades, 20 design variables define the distributions of chord, camber, blade angle, and stacking line. These distributions are also constructed using 2D Beziér curves, but for this propeller type the curves denote differences relative to a baseline design, which was obtained using the in-house propeller design tool OptoProp [15]. This design tool employs a Blade Element-Momentum method for designing propeller blades, akin to the methodology published by Adkins [16] and Drela [17]. The consequence of using an analytically designed baseline blade when optimizing is that the baseline geometry is somewhat close to the to the final, optimal blade design for a pre-specified thrust level. For the Boxprop there are no applicable analytic design methods, and therefore the design space needs to be larger to cover more possible design variations, resulting in significantly longer run times for the optimization effort.

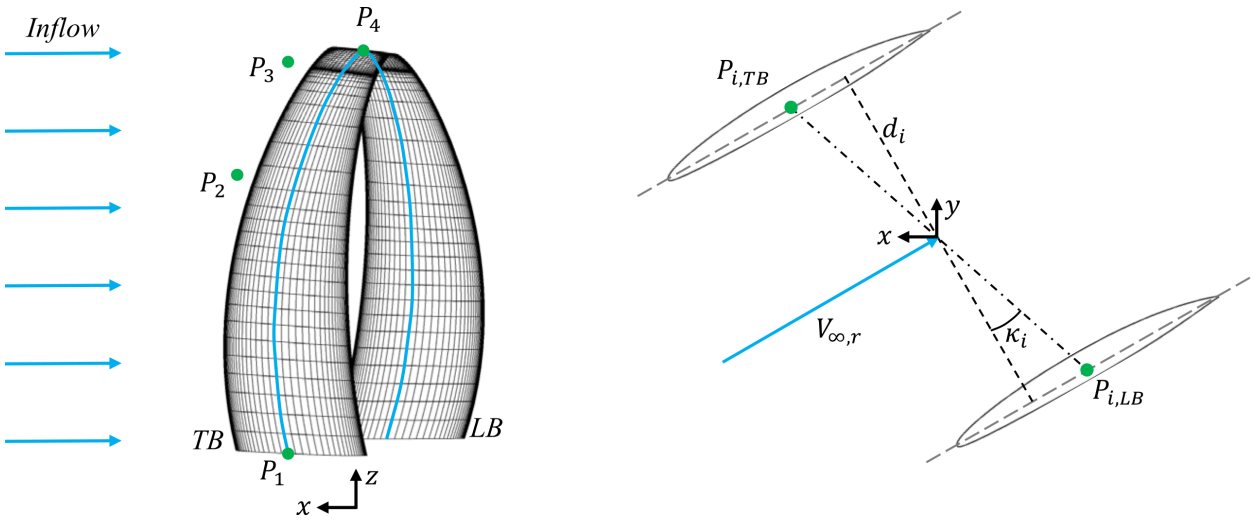

Fig. 2 Blade stacking line parametrization. Note that the LB and TB stacking lines are mirror-symmetric, so that defining one defines the other. The control points P_i for the stacking line are positioned parallel to the freestream velocity vector $V_{\infty,r}$ in the rotating frame, offset by a distance d_i and a chord displacement angle κ_i. Important to consider is that the control points P_i only intersect the stacking line at the hub, which is for point P_1. Elsewhere, the control points are positioned in the same way with d_i and κ_i, but will not necessarily coincide with the stacking line.

Table 1 Main propeller design parameters.

D, m	4.2672
HTR	0.4
n, 1/s	14.64
M_∞	0.75
h, m	10 668
$t/c\|_{root}$	6.31%
$t/c\|_{tip}$	2.15%
Airfoil	NACA16

B. Optimization framework

The multiobjective optimization platform used in this paper consists of the different components shown in Fig. 3, and is extensively described in [13]. The optimization variables affect the distributions of blade chord, camber, blade angle, and stacking line positions, while the optimization objectives are to maximize propeller efficiency and thrust coefficient.

The optimization process starts by performing an initial sampling of the design space by employing a Latin Hypercube Sampling technique. The propeller designs contained in this initial design set are then meshed and simulated using CFD. The values for propeller efficiency and thrust coefficient are extracted in post-processing, and the results from this initial design set are subsequently used to construct a meta-model by means of Radial Basis Functions. In turn, the meta-model interpolates values of thrust and efficiency for the NSGA-II [14] multiobjective Genetic Algorithm (GA). As the final step of this loop the GA outputs a pre-specified number of optimal designs, which in turn are meshed, simulated, post-processed, and added to the meta-model. This process iterates until the meta-model converges and a final Pareto front of optimal candidates is obtained.

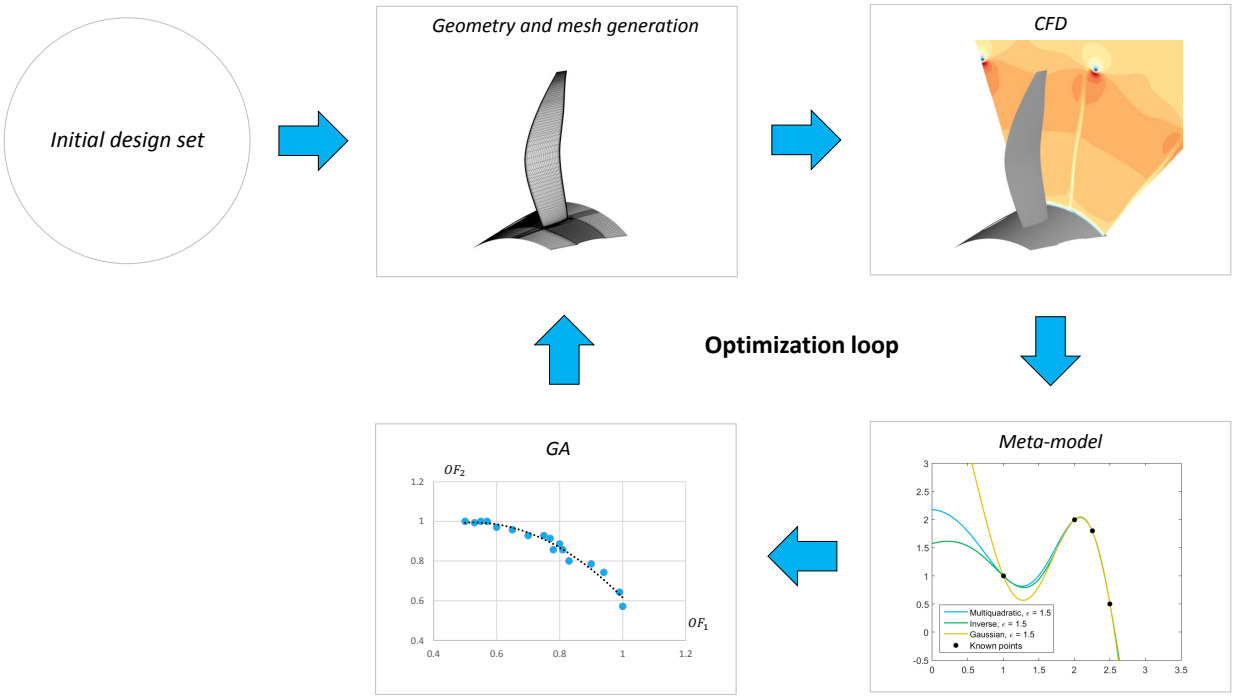

Fig. 3 Optimization platform

C. CFD methodology

ANSYS CFX 18.1 was the chosen CFD solver for the optimization effort, solving the compressible RANS-equations. The flow is set as fully turbulent, and the turbulence is accounted for using the $k-\omega$ SST turbulence model [18] coupled with a low-Re approach for the modelling of the boundary layer. Two types of domains were used for this paper, one for the optimization cases (Fig. 4a) and one for the acoustic and detailed aerodynamic analysis of the designs with thrust coefficient $C_T \approx 0.375$ (Fig. 4b). Each domain type consists of an outer quasi-2D domain and an inner 3D domain, containing one blade passage. The inner 3D domain is set as rotating, and is connected to the outer 2D domain using Frozen Rotor interfaces. Periodic boundary conditions are used to account for the periodic effects of the remaining propeller blades.

The boundary conditions are set according to Fig. 4a with total pressure, total temperature, and turbulence intensity for the inlet, and static pressure for the outlet. The opening boundary condition is set as an entrainment, which is the CFX-equivalent of a far-field boundary condition. The turbulence boundary condition is set as zero gradient turbulence for the opening boundary. In order to save computational resources for the optimization the hubs have been set as free-slip walls, while the propeller blade surface is set as a no-slip surface.

A domain and mesh study has been performed for the Boxprop in a previous paper by the authors [13], and showed small differences ($\leq 1\%$) in thrust coefficient C_T and propeller efficiency η_{prop} for mesh cell counts ranging from 0.74 to 4.25 million cells. The mesh used in this paper for the Boxprop is a modified version of the one chosen in the previously mentioned paper, and features an increased cell count in the tangential direction of the domain in order to better capture the shocks in the suction side of the blade halves, resulting in a total mesh cell count of 1.84 million. For the 6 and 12-bladed conventional propellers a similar mesh study has been performed, showing differences of less than 0.72% in thrust coefficient and 0.12% for propeller efficiency between the coarsest and finest meshes. The cell counts ranged from 1.03-3.52 million cells for the 6-bladed blade, and 0.82-2.73 million cells for the 12-bladed conventional propeller, and the final mesh sizes used was 1.03 million and 0.82 million for the 6 and 12-bladed propeller, respectively. The simulations for the acoustic and detailed aerodynamic analysis uses significantly finer mesh sizes based on the the work done in a previous paper by the authors [13], resulting in mesh counts of 48.9 million cells for the Boxprop, 29.2 million cells for the 6-bladed conventional propeller, and 14.8 million cells for the 12-bladed conventional propeller.

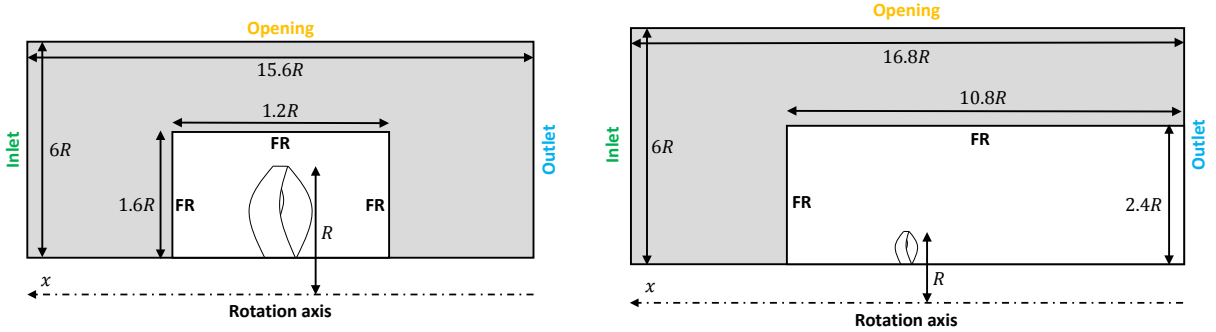

(a) Domain topology for the optimization cases.

(b) Domain topology for the acoustics and detailed analysis.

Fig. 4 Fig. 4a illustrates the domain topology for the optimization cases. The inner 3D domain contains one single rotor passage while the outer 2D domain (grey) accounts for the far-field effects. The position of the inlet, outlet, and opening boundaries is also shown. For evaluating the acoustic signatures a larger domain with finer mesh sizes was used, as is shown in Fig. 4b.

D. Acoustic methodology

The noise signature caused by the propellers investigated in this work are obtained by solving a convective form of the Ffowcs Williams - Hawkings (FW-H) equations for permeable sampling surfaces proposed by Najafi-Yazidi et al. [19]. The solution derived by these authors, known as Formulation 1C, explicitly accounts for the effects that a surrounding, uniform, mean flow has on noise radiation. This makes it possible to calculate the noise at an observer which is fixed relative to an engine in forward flight, as is done in this work. Formulation 1C expresses the noise at the observer as a surface integral over a closed surface surrounding the propellers, plus a volume integral over the exterior to the surface [19]. The integration surface does not need to represent a physical surface but can instead be placed so

that the fluid is allowed to cross it, which is why it is referred to as permeable. As noted by Di Francescantonio [20], the surface integral over a permeable surface will include the contribution from the noise generated inside the surface. The volume integral will on the other hand account for the noise generated outside the surface, as well as any effects that a nonuniform flow outside of the surface will have on wave propagation between the integration surface and the observer [20].

In this work, the volume integral is excluded from the analysis. As a consequence of this the integration surface should be placed adequately far away from the propellers to ensure that the flow outside of the surface is sufficiently uniform for there to be no significant noise generation or nonuniform wave propagation taking place here. The surface should also be constructed to ensure that the mesh used in the CFD simulation can support accurate wave propagation inside it [21, 22]. These requirements can sometimes be hard to meet in practice since the nonuniform flow field generated by a propeller can extend quite far, whereas the mesh only is kept highly resolved close to the blades in order to limit the computational cost. In this work, data is extracted from the CFD simulation on a cylinder with two end-caps in front and behind the propeller. The radius of the cylinder is chosen to be $1.05R$ and the end caps are placed one chord length upstream and downstream of the leading and trailing edge of the blade respectively. Due to the different size of the propellers, this meant that the integration surfaces were placed at different axial locations for each propeller. The motivation for doing this, compared to using a common size of all integration surfaces, was that a variable size ensures that the noise has to propagate a similar distance between the noise source (blade) and the integration surface in all cases. In order to ensure that the chosen integration surfaces would be adequate for comparing the noise of each propeller, a short sensitivity analysis was also performed for the 12-bladed conventional propeller. In this sensitivity analysis, the radius and axial locations of the original integration surface was increased twice by $0.025R$ and the noise signatures obtained from all integration surfaces were compared.

Formulation 1C has been implemented as a source time dominant algorithm [23] for integration surfaces that do not move relative to the observer. As a consequence of the latter choice, data extracted from the rotating CFD grid must be rotated and interpolated onto the stationary integration surface before the surface integral can be evaluated. The algorithm for doing this works as follows: First, surfaces in front, behind and above a single propeller are extracted from the converged CFD simulation. These surfaces are then copied and rotated to obtain a complete surface that cover the whole circumference. As the solver iterates in source time, this complete surface is rotated to the correct physical location of that time step using the rotational speed of the propeller. After this, the solution is converted to the absolute frame of reference and finally interpolated onto the stationary integration surface. The integration surface was was discretized with 1200 points in the circumferential direction, and the size of the grid in the remaining directions were chosen to obtain the same grid spacing in these directions as well. The sampling rate was chosen to be $400 \cdot n \cdot B$ Hz, i.e. 400 times the blade passing frequency of the propeller. The chosen sampling rate and grid spacing well covered the largest frequency and corresponding smallest wavelength that were observed in the noise spectra. Some more details on the implementation of the acoustic methodology used in this work, including a description for how it can be used in case the flow is modeled using the Harmonic Balance method [24], can be found in [25]

III. Results

A. Optimal designs

Overall results for the aerodynamic optimizations of the Boxprop and the conventional propellers are shown in Fig. 5. Fig. 5d includes the performance values for the three chosen propellers with $C_T \approx 0.375$, which have been simulated with finer meshes than during the optimizations. Because of the larger inner domain and the refined meshes, the efficiency values have changed for all three designs. The refined simulations show that the Boxprop propeller efficiency is slightly higher than the efficiency obtained for the 6-bladed propeller, but lower than for the 12-bladed propeller. The relatively small improvement in propeller efficiency for the Boxprop relative to the 6-bladed propeller reflects a number of challenges faced while optimizing the complex shape of the Boxprop:

- The higher number of design variables (32 versus 20) for the Boxprop compared to the conventional propellers.
- The coupled nature of the blade halves. Whenever a design parameter in one blade half changes, it will also affect the performance of other blade half to some degree.
- The lack of an analytically derived initial guess - there is no analytical method for producing minimum-induced loss Boxprop designs, which necessitates the use of 3D CFD and aerodynamic optimization.

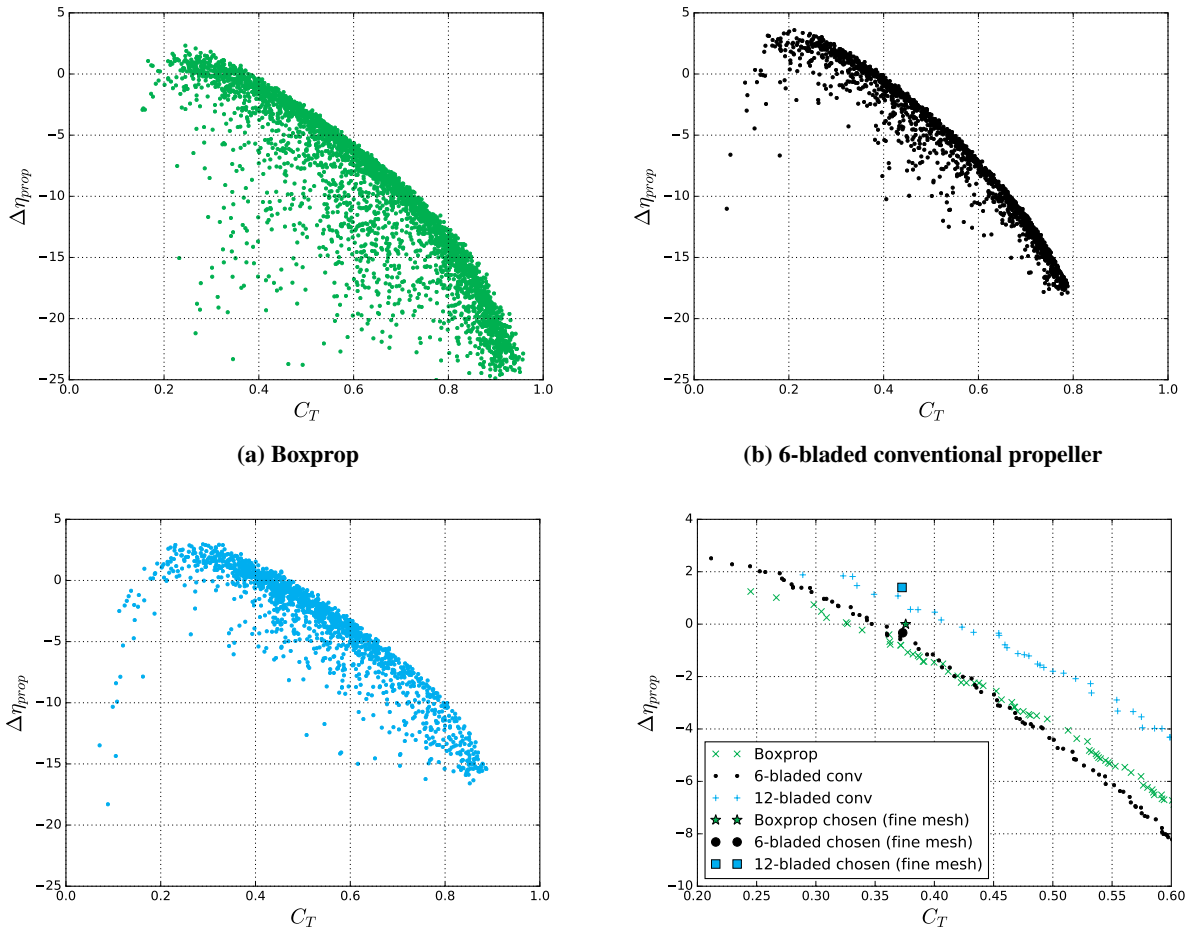

(a) Boxprop

(b) 6-bladed conventional propeller

(c) 12-bladed conventional propeller

(d) Pareto fronts all of three 3 optimizations.

Fig. 5 Objective function values for the optimizations of (a) the Boxprop, (b) the 6-bladed conventional propeller, and (c) the 12-bladed conventional propeller. The Pareto fronts of all three optimizations have been plotted in Fig 5d. The propeller efficiencies have been normalized using the Boxprop propeller efficiency at $C_T = 0.375$.

B. Blade section performance

The sectional thrust produced at different radial cuts of the propellers is shown in Fig. 7 together with the sectional lift and lift-to-drag ratios for all three designs. The location of peak thrust of the Boxprop lies between the 12-bladed and the 6-bladed conventional propeller. The 12-bladed propeller produces thrust further out radially when compared to the 6-bladed due to its higher aspect ratio, while the Boxprop produces less thrust at the tip due to its arc-shaped tip. At the absolute tip of the Boxprop the lift vector is parallel with the radial direction resulting no contribution from lift to thrust. Instead the only contribution comes from drag, which yields negative thrust at the tip for the Boxprop. Another major difference is the lift-to-drag ratios of the Boxprop, whose values match the ones for the conventional propellers from 50% to 80% of the tip radius. Outside this area the Boxprop lift-to-drag ratio is seen to decrease. The area of low lift-to-drag ratio at the hub is due to blade interference; the proximity of the blades decreases the amount of obtainable lift on the TB, which is compensated by higher lift on the LB, as is seen in 7. The angle-of-attack at the 50% radial position of the LB (not shown here) is 3.2 degrees higher than for the TB, which is consistent with the higher lift and the decreased lift-to-drag ratio experienced by the LB. For the tip it is important to consider that the parametrization employed in this paper pre-defines the tip angle-of-attack and camber to zero, leading to low amounts of lift and low lift-to-drag ratios due to the transonic nature of the flow at the tip.

The Mach number contours have been plotted at the 75% and 90% radial positions for all three propellers in Fig. 6. Here it is evident why the Boxprop blade halves need to be sheared apart, so that the low pressure regions of the

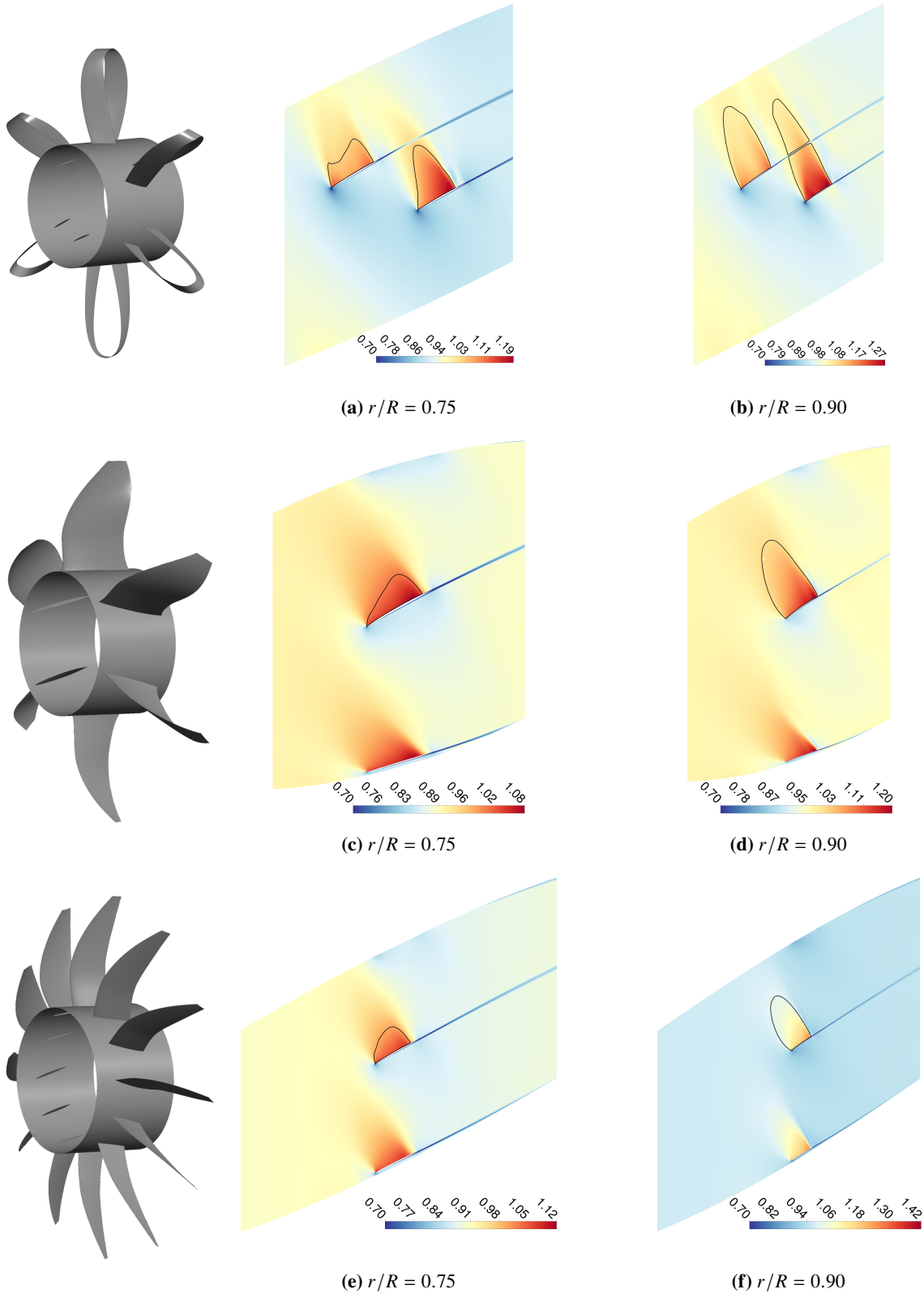

(a) $r/R = 0.75$ **(b)** $r/R = 0.90$

(c) $r/R = 0.75$ **(d)** $r/R = 0.90$

(e) $r/R = 0.75$ **(f)** $r/R = 0.90$

Fig. 6 Mach number at the 75% and 90% radial positions for the Boxprop, 6-bladed, and 12-bladed conventional propellers. The black lines denote regions of Mach equal to unity.

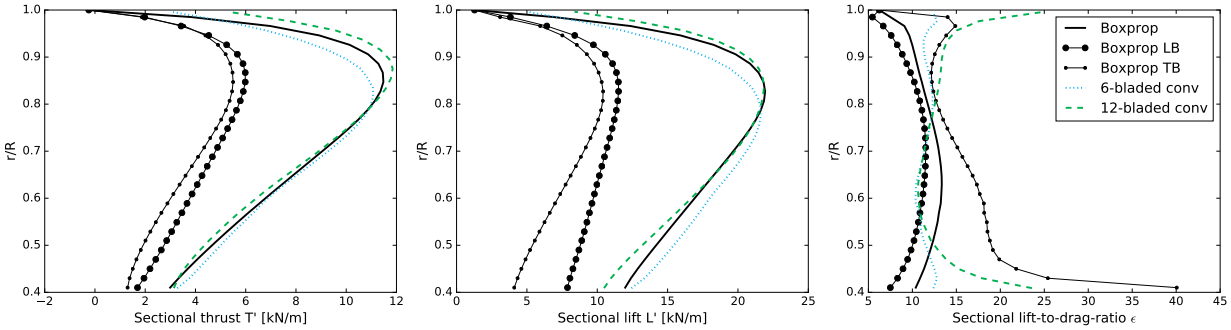

Fig. 7 Sectional performance in terms of thrust, lift, and lift-to-drag ratios for the three analyzed propellers.

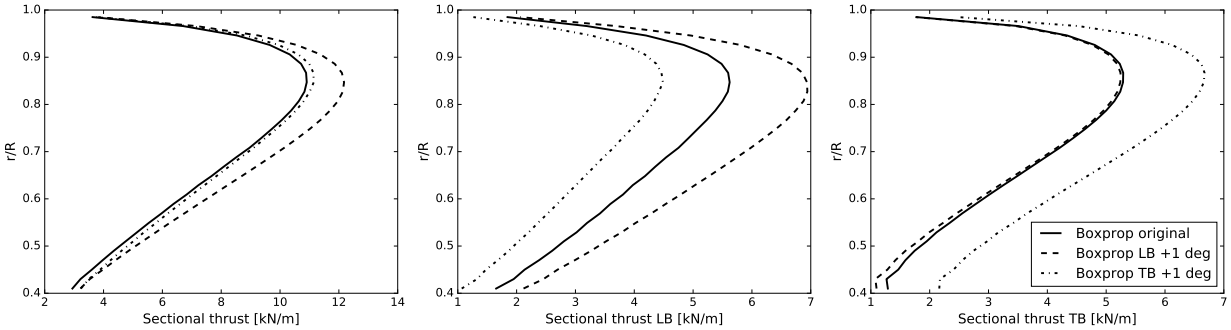

Fig. 8 Sectional thrust for the optimized Boxprop and two modified design cases. The first case features an increased angle-of-attack on the LB while keeping the original TB angle-of-attack distribution. The second case modifies the TB angle-of-attack distribution while keeping the original LB.

suction sides of each blade half can propagate freely in space. The optimization has resulted in relatively weak shocks positioned at the trailing edges of each blade, which improves the aerodynamic efficiency. The highest Mach number is 1.4, and can be found in a small area on the suction side close to the leading edge of the 12-bladed propeller at the 90% radius. A noteworthy feature is how the wake of the trailing blade cuts through the high Mach number area of the leading blade suction side. These figures also highlight the coupled nature of the performance of the blade halves. If the optimizer changes the blade angle of one blade half, the flow conditions change for the other blade half as well, including the angle-of-attack, thrust, and lift. As was noted by Zachariadis [26], high-speed, low camber propeller blades are highly sensitive to changes in angle-of-attack. This was illustrated by changing the blade angle of the front rotor of a counter-rotating open rotor by 1°, which increased its thrust and power by more than 15%. This means that relatively small changes in angles-of-attack are required for fine-tuning the performance of a high-speed propeller blade, which is made more challenging because of the coupled nature of the Boxprop blade halves. In order to assess the sensitivity of changes in angle-of-attack for the Boxprop two cases were prepared were the angle-of-attack was changed in one blade half at a time relative to the original design. For the first case, the angle-of-attack distribution of the TB is kept as in the original Boxprop blade while the LB angle-of-attack was increased with 1° between the hub and the 90% radial position. After this position the addition of angle-of-attack decreased smoothly towards zero at the tip of the blade. The second case simply did the opposite, added 1° to the TB angle-of-attack distribution while keeping the original distribution on the LB. The resulting radial thrust distributions can be seen in Fig. 8. Adding 1° to the LB increased overall thrust by 11%, which resulted in an increase in LB thrust by 24% and a decrease in thrust in the TB by 2.3%. For the second case 1° was added to the TB, which increased overall thrust with 3%. The LB thrust decreased by 23.5% while the TB thrust increased with 34%. In essence, changes in angle-of-attack of the trailing blade have a substantially larger effect on the performance of the LB then the other way around. For this case, the sought after thrust increase when increasing the angle-of-attack of the TB is almost entirely diminished by the thrust decrease on the LB.

C. The propeller wake

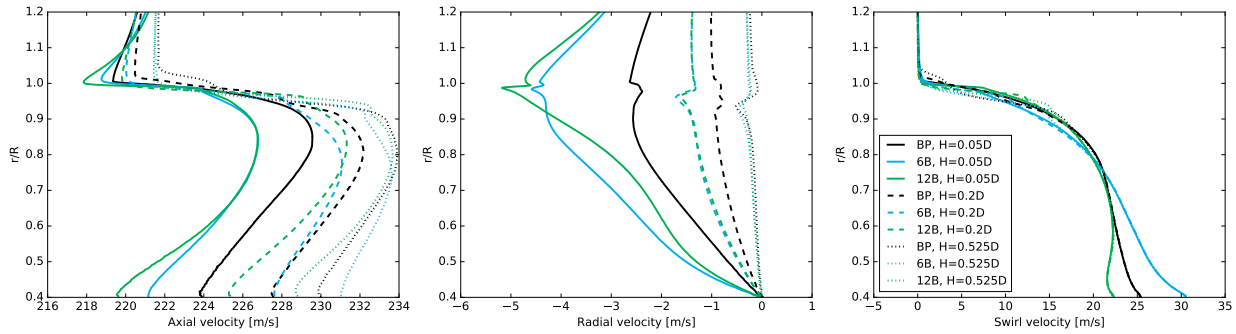

Fig. 9 Circumferentially averaged axial, radial, and swirl velocities for the three analyzed propellers at three downstream positions H. Boxprop is denoted as BP, the 6-bladed conventional propeller as 6B, and the 12-bladed as 12B.

The circumferentially averaged axial, radial and swirl velocities at three distances downstream from the 75% radial position of each blade is shown in Fig. 9. The distances H are have been chosen to represent the wake close to the propellers ($H = 0.05D$), at a downstream distance where a modern CROR would located its rear, counter-rotating propeller ($H = 0.2D$), and a far downstream position ($H = 0.525D$) where most of pressure increase in the propeller disk has been transformed into axial kinetic energy. In Fig. 9 one can see that the axial velocity in the jet is higher for the Boxprop compared to the two conventional propellers close to the propeller ($H = 0.05D$), but that further downstream they achieve the same jet axial velocity. The fact that they reach the same jet velocity far downstream is expected since they produce very similar levels of thrust, while the higher axial velocity for the Boxprop near its trailing edge is connected to how its blade halves are swept. The simple *actuator disk theory* for propellers is based on the assumption that there is a continuous increase in axial velocity and discontinuous increase in pressure when the flow passes through a propeller. Therefore, a jet forms downstream of the propeller where pressure energy is transformed into axial kinetic energy. For a Boxprop, the formation of the jet and the associated transfer of energy from pressure to axial kinetic energy is started further upstream than it is for the conventional propellers because of how the Boxprop blade halves are swept in opposite directions. The radial velocities seen in Fig. 9 are negative due to the slipstream contraction, and the kinks in the velocity profiles near the tip of the blades are the tip vortices of the conventional blades.

An important flow feature with regards to performance for a single propeller is the amount of swirl in the propeller wake. In a counter-rotating open rotor swirl is recoverable and can be turned into thrust, but for a single propeller it is instead considered a loss. In Fig. 9 it can be seen that Boxprop lies somwhere in between the 6 and 12-bladed conventional propeller in terms of swirl, and produces more swirl than the 12-bladed propeller in the lower half of the blade. The amount of shaft power converted to swirl is 7.81% for the Boxprop, 8.53% for the 6-bladed conventional propeller, and 7.36% for the 12-bladed propeller at a downstream distance of $0.2D$.

Contours of the swirl velocity in the stationary reference frame at a plane located $0.2D$ downstream of the blades is shown in Fig. 10. The largest velocity magnitudes are observed for the tip vortex of the 6-bladed conventional propeller, while the lowest magnitude is found for the Boxprop. As expected, the tip vortex of the 12-bladed propeller features lower velocities than for the 6-bladed conventional propeller, which is confirmed with values of the vorticity magnitude, as shown in Fig. 11. There seems to be a vortex-like structure in the wake of the Boxprop, but it is 32% and 20% weaker than the vortex of the 6 and 12-bladed conventional propeller, respectively.

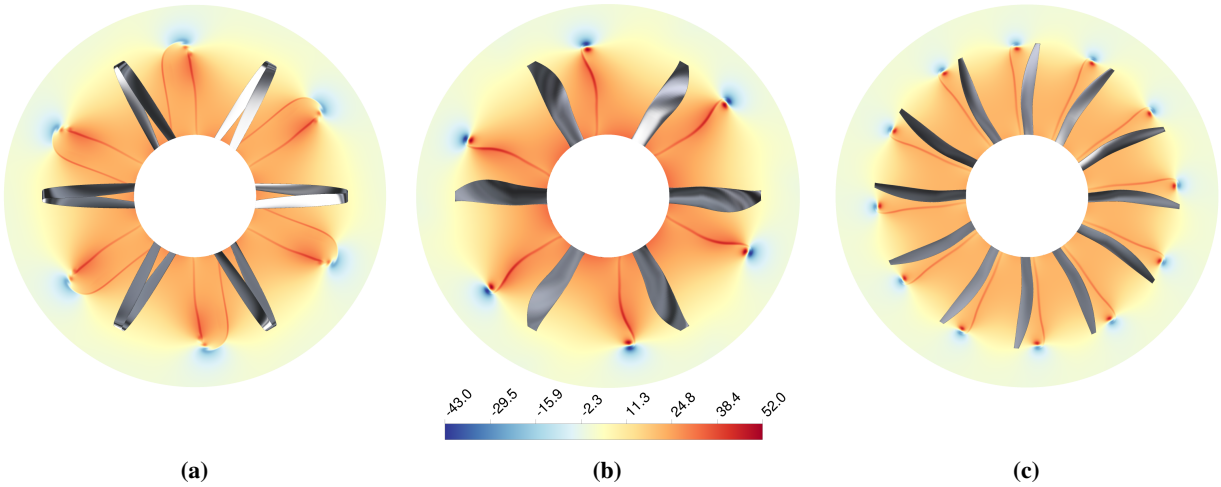

Fig. 10 Swirl velocities v_θ [m/s] for the a) 6-bladed Boxprop $[-23.7, 40.6]$, b) the 6-bladed $[-43.0, 52.0]$, and c) 12-bladed conventional propeller $[-26.8, 45.3]$ on planes at a distance of $0.2D$ from the trailing edges of the 75% radial position of the blades.

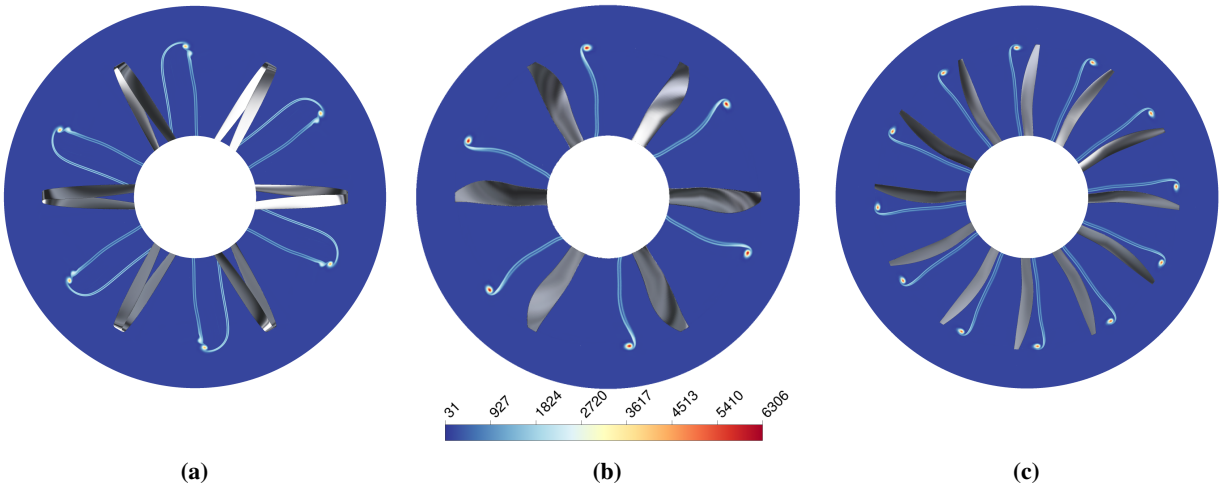

Fig. 11 Vorticity magnitude [1/s] for the a) 6-bladed Boxprop $[60, 4286]$, b) the 6-bladed $[62, 6306]$, and c) 12-bladed conventional propeller $[31, 5357]$ on planes at a distance of $0.2D$ from the trailing edges of the 75% radial position of the blades.

D. Acoustic results

The noise signature of all three propellers investigated in this work has been computed for a set of near field and far field observers. The near field observers were placed on a circular arc with radius $r = 2D$ whereas the far field observes were placed at $r = 10D$ instead. The near field results are presented in Fig. 12 in terms of sound pressure level (SPL) directivity plots. Note that $\theta = 0°$ and $\theta = 180°$ represent the upstream and downstream direction respectively. From Fig. 12 it can first be noted that the noise of all three propellers peaks around $\theta = 90°$. This is typical for an isolated propeller for which the radiation efficiency decays quickly for low and high polar angles [27]. It is also interesting to note that the noise levels generally are higher for the two 6-bladed propellers compared to the 12-bladed propeller. The cause of this difference will be discussed in further detail later when the total SPL levels for all propellers are compared back to back. A final thing that can be noted in Fig. 12a is that there are two distinct peaks in the SPL spectra for the

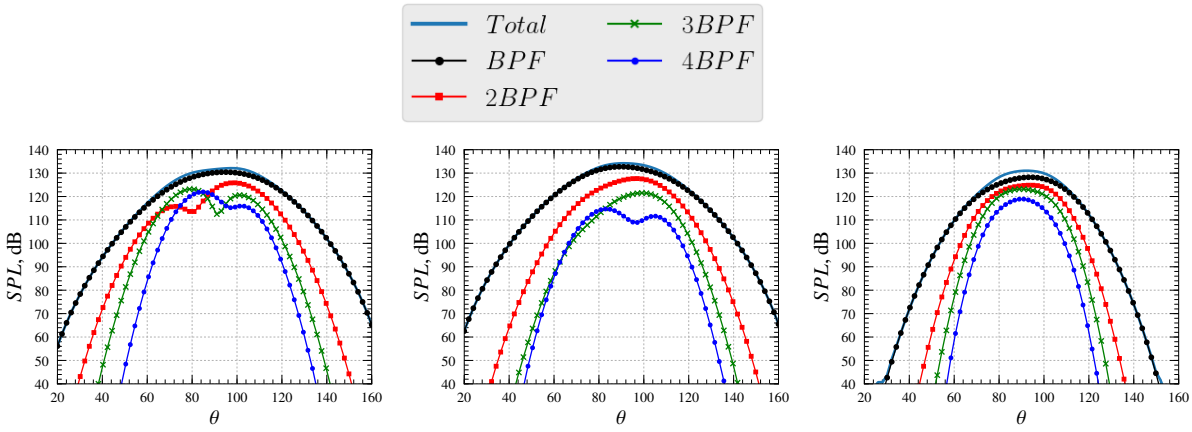

(a) 6-bladed Boxprop propeller. **(b) 6-bladed conventional propeller.** **(c) 12-bladed conventional propeller.**

Fig. 12 Nearfield noise directivity with FW-H surfaces placed at $r = 1.05R$.

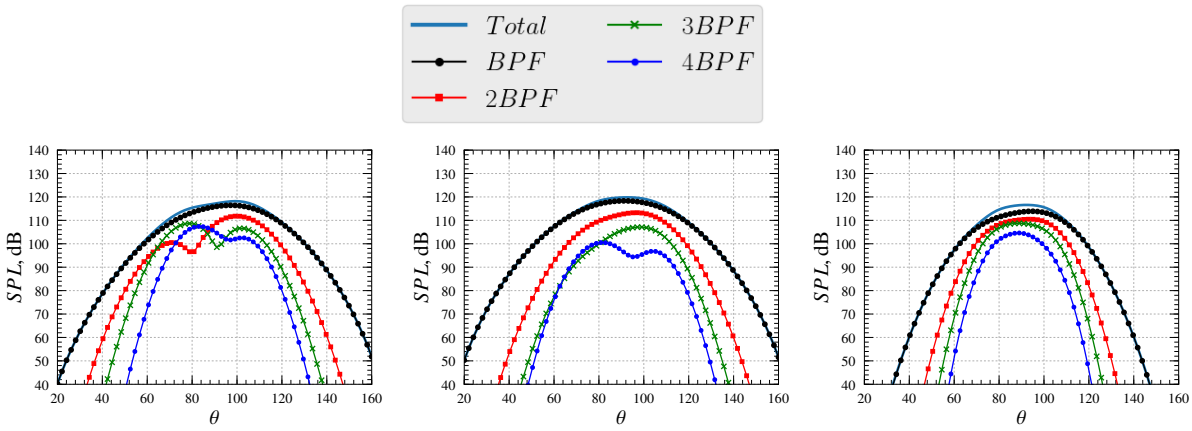

(a) 6-bladed Boxprop propeller. **(b) 6-bladed conventional propeller.** **(c) 12-bladed conventional propeller.**

Fig. 13 Farfield noise directivity with FW-H surfaces placed at $r = 1.05R$.

higher frequencies of the Boxprop propeller. These are believed to appear due to the fact that the leading and trailing blade of the Boxprop radiate noise in different directions. The reason for why two distinct peaks only appear for the higher frequencies is further believed to be due to that the leading and trailing blade of the Boxprop no longer form one single acoustically compact source for higher frequencies/shorter wavelengths.

The far field noise signature of the three propellers are presented in Fig. 13. The results in this figure are almost identical to those in Fig. 12 apart from that the noise levels are lower due to the increased distance between the noise source and the observers.

In Fig. 14 the change in the near field noise signature obtained from increasing the size of the integral surface is presented for the 12-bladed conventional propeller. From this figure it can be seen that the total SPL levels remain essentially the same, whereas some differences can be observed for the higher frequencies. It is hard to say exactly why the differences occur. One reason may be that the propellers investigated in this work all are transonic, which causes a shock to extend quite far radially above the blades. As a consequence of this, the entire shock is not enclosed by an integral surface with radius $r = 1.05R$, and extending the surface thus implies that more nonlinear effects are included into the acoustic analysis. Another cause of the differences may be that the grids used in the CFD computations were not optimized for acoustic purposes, which may yield some additional dissipation and dispersion errors when the integral surface is extended. Despite this, the results obtained from the sensitivity analysis indicate that the acoustic methodology

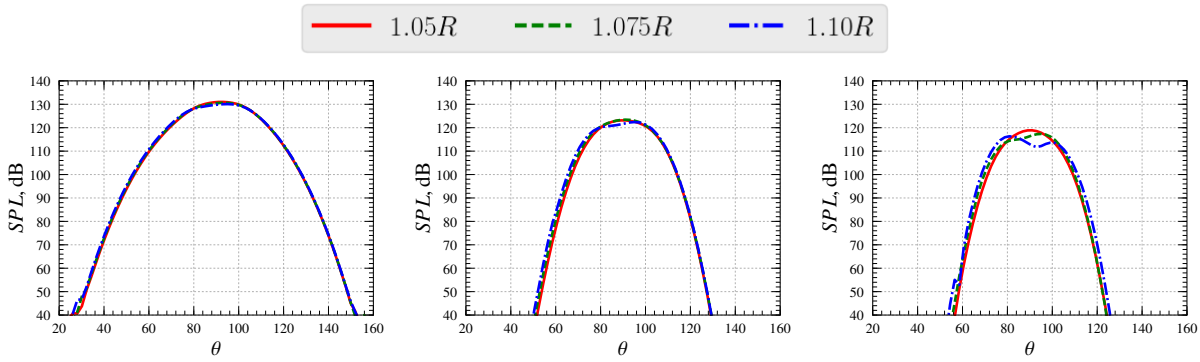

(a) Total Sound Pressure Level. **(b) Third blade passing frequency.** **(c) Fourth blade passing frequency.**

Fig. 14 Nearfield noise directivity for the 12-bladed conventional propeller with FW-H surfaces at $r = 1.05R, 1.075R$ and $1.10R$.

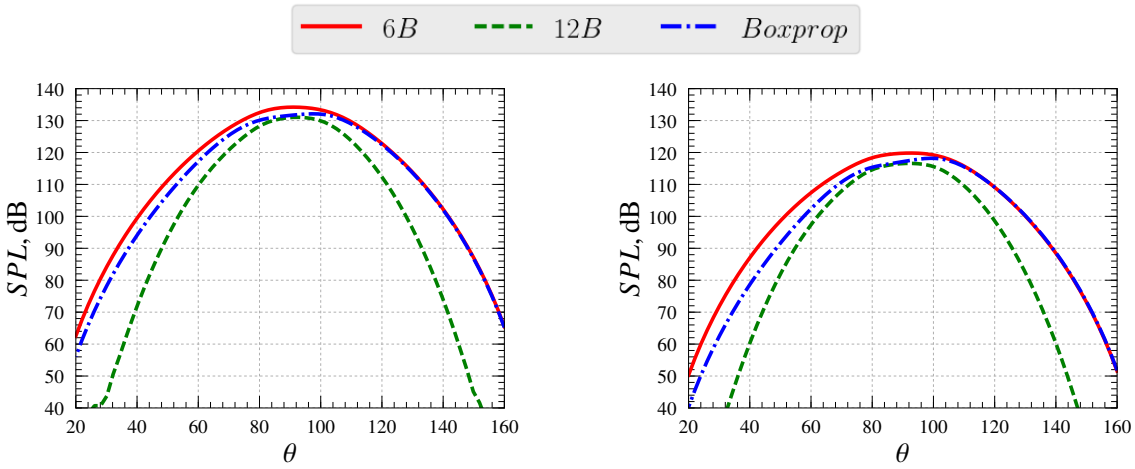

(a) Nearfield. **(b) Farfield.**

Fig. 15 Comparison of noise directivity for all propellers with FW-H surfaces placed at $r = 1.05R$.

used in this work is robust enough to be used for comparing all three propellers back to back, as will be done next.

The total SPL levels obtained for all three propellers are presented back to back for the near and far field observes in Fig. 15. The results in this figure show that the 12-bladed conventional propeller produces the lowest noise levels, followed by the Boxprop and the 6-bladed conventional propeller. According to the acoustic formulas derived for a single propeller by Hanson [27], the radiation efficiency in a particular direction should be similar for all three propellers since it is only governed by the tangential Mach number of a blade section, which in turn is the same for all propellers. Instead, it is believed that the difference in noise levels comes from the fact that the efficiency of the 12-bladed conventional propeller is the highest, followed by the Boxprop and the 6-bladed conventional propeller. This difference in efficiency leads to a higher torque for a constant C_T, which in turn means larger blade forces and thereby more noise generation.

IV. Conclusions

The optimization framework in this paper has successfully produced a large number of optimal Boxprop and conventional blade designs. Three designs were chosen from the Pareto fronts of the optimizations, and they all share some common features which has lead to high efficiency, namely low Mach numbers and weak shocks in the suction sides of the blades, shocks positioned near the trailing edge of the blades, and sectional thrust distributions which peak

at high radii.

The propeller efficiency of the analyzed, optimized Boxprop geometry seems to lie in-between the levels of the 6 and 12-bladed conventional blades, mostly due the fact that the 12-bladed propeller has its sectional thrust peak at higher radii and produces less swirl. The Boxprop design has some remaining interference at the hub and its blade tip does not provide thrust with the current parametrization, two factors which can explain the slightly higher efficiency of the 12-bladed conventional blade. These loss sources can potentially be decreased by adjusting the blade parametrization to allow for more design variation at the blade tip. With regards to the optimization process itself, the process is more challenging for the Boxprop than for a conventional blade for several reasons:

- The higher number of design variables required for the Boxprop.
- The lack of a decent initial guess or baseline design for the Boxprop.
- The performance of the Boxprop blade halves is coupled - This was seen by varying the angle-of-attack dist of the LB and TB separately. Changes in the TB angle-of-attack distribution affects the performance of both the TB and LB, while changing the LB angle-of-attack distribution only affects the LB itself.

The optimized Boxprop geometry is swept both upstream and downstream, depending on which blade half is considered. An interesting consequence of the TB being swept upstream is that the jet is formed further upstream than for the conventional propeller, leading to higher axial velocities in regions close to the blade. The axial velocity at the downstream location of $0.2D$, corresponding to the placement of a rear, counter-rotating blade (as in a CROR) features small differences in velocity, so the effect on the rear blade design should be small. Also, the magnitude of the radial velocity is considerably smaller for the Boxprop than for the other designs.

The Boxprop produces more swirl than the 12-bladed propeller but less than the 6-bladed conventional one, but the minimum and maximum swirl velocities are lower for the analyzed Boxprop. The maximum swirl velocities occur in the tip vortex regions of the conventional blades, while for the Boxprop it is along the wake of the TB. Vorticity plots show the presence of a small vortex-like flow feature in the wake of the Boxprop, but its strength is weaker than the tip vortices found in the conventional blades. The existence of this vortex and its effect on acoustics during takeoff conditions remains to be seen.

The acoustic analysis revealed that the permeable Ffowcs Williams - Hawkings methodology used in this work was fairly robust to the placement of the integration surface. This in turn enabled a reliable comparison between all three propellers to be done, despite the fact that the size of the integral surfaces were different for each propeller. The comparison showed that the 12-bladed conventional propeller produced the lowest noise levels, followed by the Boxprop and the 6-bladed conventional propeller. It is believed that this result can be explained by the fact that the propeller efficiencies rank in the same way from highest to lowest for the particular C_T chosen in this work. This in turn means that the 6-bladed conventional propeller produces the most torque, followed by the Boxprop and the 12-bladed conventional propeller, which in turn means more noise due to a higher blade loading. If this hypothesis is true, and considering the fact that no significant differences were observed in the noise signature of each propeller type other than absolute levels, it can be concluded that the efficiency is a good common factor for predicting which propeller that will give the lowest noise in cruise. Considering the fact that the 6-bladed conventional propeller and the 6-bladed Boxprop gives fairly equal efficiencies across a large range of thrust coefficients according to Fig. 5d, the above argument would then imply that the 6-bladed Boxprop is competitive with a 6-bladed conventional propeller with respect to noise in cruise. The 12-bladed conventional propeller does on the other hand appear to have an edge on the 6-bladed ones across all the investigated thrust coefficients according to Fig. 5d. It must however be kept in mind that the main purpose of the Boxprop with respect to noise is to reduce the strength of the tip vortex compared to a conventional propeller, thereby hopefully minimizing interaction noise when used as a front rotor in a CROR. Whether this is the case at take-off and approach conditions, where noise certainly is of most relevance, remains to be investigated in the future.

V. Acknowledgments

This work is financed and supported by Sweden's National Aeronautics Research Programme (NFFP), sponsored jointly by the Swedish Armed Forces, the Swedish Defense Material Administration and the Swedish Governmental Agency for Innovation Systems. The work was also financially supported by the E.U. under the ULTIMATE Project funded by the European Commission within the Horizon 2020 Programme (2014-2020) under the Grant Agreement No 633436. The authors would also like to acknowledge the Swedish National Infrastructure for Computing (SNIC) for providing computer resources at the Chalmers Centre for Computational Science and Engineering (C3SE) in Gothenburg, Sweden.

References

[1] Larsson, L., Gronstedt, T., and Kyprianidis, K. G., "Conceptual design and mission analysis for a geared turbofan and an open rotor configuration," *ASME 2011 Turbo Expo: Turbine Technical Conference and Exposition*, American Society of Mechanical Engineers, 2011, pp. 359–370.

[2] Van Zante, D. E., Collier, F., Orton, A., Khalid, S. A., Wojno, J. P., and Wood, T. H., "Progress in open rotor propulsors: The FAA/GE/NASA open rotor test campaign," *The Aeronautical Journal*, Vol. 118, No. 1208, 2014, pp. 1181–1213.

[3] Peters, A., and Spakovszky, Z. S., "Rotor interaction noise in counter-rotating propfan propulsion systems," *Journal of Turbomachinery*, Vol. 134, No. 1, 2012, p. 011002.

[4] Negulescu, C. A., "Airbus AI-PX7 CROR design features and aerodynamics," *SAE International Journal of Aerospace*, Vol. 6, No. 2013-01-2245, 2013, pp. 626–642.

[5] Hall, C., Zachariadis, A., Brandvik, T., and Sohoni, N., "How to improve open rotor aerodynamics at cruise and take-off," *The Aeronautical Journal*, Vol. 118, No. 1208, 2014, pp. 1103–1123.

[6] Zachariadis, A., Hall, C., and Parry, A. B., "Contrarotating open rotor operation for improved aerodynamics and noise at takeoff," *Journal of Turbomachinery*, Vol. 135, No. 3, 2013, p. 031010.

[7] Lepot, I., Leborgne, M., Schnell, R., Yin, J., Delattre, G., Falissard, F., and Talbotec, J., "Aero-mechanical optimization of a contra-rotating open rotor and assessment of its aerodynamic and acoustic characteristics," *Proceedings of the Institution of Mechanical Engineers, Part A: Journal of Power and Energy*, Vol. 225, No. 7, 2011, pp. 850–863.

[8] Schnell, R., Yin, J., Voss, C., and Nicke, E., "Assessment and optimization of the aerodynamic and acoustic characteristics of a counter rotating open rotor," *Journal of Turbomachinery*, Vol. 134, No. 6, 2012, p. 061016.

[9] Jaron, R., Moreau, A., Guérin, S., and Schnell, R., "Optimization of Trailing-Edge Serrations to Reduce Open-Rotor Tonal Interaction Noise," *Journal of Fluids Engineering*, Vol. 140, No. 2, 2018, p. 021201.

[10] Avellán, R., and Lundbladh, A., "Boxprop, a forward-swept joined-blade propeller," *ISABE-2013-1108*, 2013.

[11] Avellán, R., Capitao Patrao, A., Lundbladh, A., and Grönstedt, T., "Preparing for Proof-of-concept of a Novel Propeller for Open Rotor Engines," *ISABE-2015-20097*, 2015.

[12] Patrao, A. C., Avellán, R., Lundbladh, A., and Grönstedt, T., "Wake and Loss Analysis for a Double Bladed Swept Propeller," *ASME Turbo Expo 2016: Turbomachinery Technical Conference and Exposition*, American Society of Mechanical Engineers, 2016, pp. V001T01A013–V001T01A013.

[13] Capitao Patrao, A., Grönstedt, T., Avellán, R., Lundbladh, A., and Montero Villar, G., "An Optimization Platform for High Speed Propellers," *Swedish Aerospace Technology Congress 2016*, 2016.

[14] Deb, K., Pratap, A., Agarwal, S., and Meyarivan, T., "A fast and elitist multiobjective genetic algorithm: NSGA-II," *IEEE transactions on evolutionary computation*, Vol. 6, No. 2, 2002, pp. 182–197.

[15] Capitao Patrao, A., "Implementation of Blade Element Momentum/Vortex Methods for the Design of Aero Engine Propellers," Tech. rep., 2017. 30.

[16] Adkins, C. N., and Liebeck, R. H., "Design of optimum propellers," *Journal of Propulsion and Power*, Vol. 10, No. 5, 1994, pp. 676–682.

[17] Drela, M., "QPROP formulation," *Massachusetts Inst. of Technology Aeronautics and Astronautics, Cambridge, MA*, 2006.

[18] ANSYS, C., "Solver Theory Guide," *ANSYS CFX Release*, Vol. 15, 2013.

[19] Najafi-Yazidi, A., Brès, G. A., and Mongeau, L., "An Acoustic Analogy Formulation for Moving Sources in Uniformly Moving Media," *Proceedings of the Royal Society A, Mathematical, Physical and Engineering Sciences*, Vol. 467, No. 2125, 2011, pp. 144–165.

[20] di Francescantonio, P., "A New Boundary Integral Formulation for the Prediction of Sound Radiation," *Journal of Sound and Vibration*, Vol. 202, No. 4, 1997, pp. 491–509.

[21] Farassat, F., "Derivation of Formulations 1 and 1A of Farassat," Technical Report NASA/TM-2007-214853, NASA, Hampton, VA, March 2007.

[22] Farassat, F., "Open Rotor Noise Prediction at NASA Langley - Capabilities, Research and Development," Technical Report NASA/TM-2010-216178, NASA, Hampton, VA, January 2010.

[23] Brentner, K. S., and Farassat, F., "Modeling aerodynamically generated sound of helicopter rotors," *Progress in Aerospace Sciences*, Vol. 39, No. 2-3, 2003, pp. 83–120.

[24] Hall, K. C., Jeffrey, P. T., and Clark, W. S., "Computation of Unsteady Nonlinear Flows in Cascades Using a Harmonic Balance Technique," *AIAA Journal*, Vol. 40, No. 5, 2002, pp. 879–886.

[25] Lindblad, D., Montero Villar, G., Andersson, N., Capitao Patrao, A., Courty-Audren, S.-k., and Napias, G., "Aeroacoustic Analysis of a Counter Rotating Open Rotor based on the Harmonic Balance Method," *2018 AIAA Aerospace Sciences Meeting*, AIAA Paper 2018-1004, 2018.

[26] Zachariadis, A., and Hall, C. A., "Application of a navier–stokes solver to the study of open rotor aerodynamics," *Journal of Turbomachinery*, Vol. 133, No. 3, 2011, p. 031025.

[27] Hubbard, H. H. (ed.), *Aeroacoustics of Flight Vehicles*, Vol. 1, Acoustical Society of America, 1995. Noise Sources.